J. Cent. South Univ. (2018) 25: 1987−2001
DOI: https://doi.org/10.1007/s11771-018-3889-2

Springer

Experimental investigation on deformation characteristics and permeability evolution of rock under confining pressure unloading conditions

CHEN Xu(陈旭)[1], TANG Chun-an(唐春安)[1, 2], YU Jin(俞缙)[3],
ZHOU Jian-feng(周建烽)[3], CAI Yan-yan(蔡燕燕)[3]

1. School of Resources and Civil Engineering, Northeastern University, Shenyang 110819, China;
2. School of Civil and Hydraulic Engineering, Dalian University of Technology, Dalian 116024, China;
3. Fujian Research Center for Tunneling and Urban Underground Space Engineering, Huaqiao University, Xiamen 361021, China

Abstract: Deformation behavior and hydraulic properties of rock are the two main factors that influence safety of excavation and use of rock engineering due to in situ stress release. The primary objective of this study is to explore deformation characteristics and permeability properties and provide some parameters to character the rock under unloading conditions. A series of triaxial tests with permeability and acoustic emission signal measurement were conducted under the path of confining pressure unloading prior to the peak stress. Deformation behavior and permeability evolution in the whole stress–strain process based on these experimental results were analyzed in detail. Results demonstrate that, under the confining pressure unloading conditions, a good correspondence relationship among the stress–axial strain curve, permeability–axial strain curve and acoustic emission activity pattern was obtained. After the confining pressure was unloaded, the radial strain grew much faster than the axial strain, which induced the volumetric strain growing rapidly. All failures under confining pressure unloading conditions featured brittle shear failure with a single macro shear rupture surface. With the decrease in deformation modulus during the confining pressure unloading process, the damage variable gradually increases, indicating that confining pressure unloading was a process of damage accumulation and strength degradation. From the entire loading and unloading process, there was a certain positive correlation between the permeability and volumetric strain.

Key words: unloading rock mechanics; permeability evolution; triaxial experiment; acoustic emission; sandstone

Cite this article as: CHEN Xu, TANG Chun-an, YU Jin, ZHOU Jian-feng, CAI Yan-yan. Experimental investigation on deformation characteristics and permeability evolution of rock under confining pressure unloading conditions [J]. Journal of Central South University, 2018, 25(8): 1987–2001. DOI: https://doi.org/10.1007/s11771-018-3889-2.

1 Introduction

With the development of some challenging issues, such as underground nuclear waste disposal [1–4], CO_2 storage systems [5, 6], extraction of gas, oil and mineral resources from deep earth, excavation of dam foundation and deep buried tunnels [7, 8], rock engineering under coupled high geostress and high groundwater pressure are commonly encountered. Excavation in such deep rocks increases the risk of some engineering disasters, including rock burst, water inrush, etc., since unloading may induce serious damage or even

Foundation item: Project(2014CB047100) supported by the National Basic Research Program of China (973 Program); Projects(51679093/E090705, 51774147/E0409) supported by the National Natural Science Foundation of China; Project(2017J01094) supported by the Natural Science Foundation of Fujian Province, China
Received date: 2017−03−06; **Accepted date:** 2017−09−24
Corresponding author: TANG Chun-an, PhD, Professor; Tel: +86–411–84978785; E-mail: tca@mail.neu.edu.cn; ORCID: 0000-0001-8284-0211

failure of rock. Thus, the researches of the deformation behavior and hydraulic properties of rock under geostress unloading conditions maintain a significant and hot topic in rock mechanics.

Traditionally, the mechanical characteristics of rock were primarily focused on conventional triaxial compression [9–13]. However, the unloading behaviors of rock deformation and failure are substantially different from the behaviors under loading conditions. In the past few years, many scholars have made continuing and intensive efforts on studying unloading characteristics of rock. HUANG et al [14] and HUA et al [15] designed a series of triaxial unloading tests to simulate the unloading process during tunnel excavation, and reported the variation laws of unloading deformation parameters (strength, unloading deformation modulus, Poisson ratio, and damage variants) and their characteristics through the full process of stress–strain tests under loading and unloading conditions. Also, LIU et al [16] investigate the effect of confining pressure unloading on soft coal strength reduction for borehole stability analysis by conducting a series of mechanical tests under loading paths of conventional uniaxial/triaxial compression and triaxial compression with confining pressure unloading, leading to a significant reduction in coal strength due to confining pressure unloading. To investigate the effects of the confining pressure and the loading and unloading cycles on the mechanical properties of the rock in the residual phase, LIANG et al [17] carried out some experiments on argillaceous limestone specimens, resulting in a fact that the bearing capacity is related to loading path. HUANG et al [18] performed some axisymmetric triaxial compression loading–unloading tests on marble samples with different initial confining pressures and unloading rates. It is found that the failure modes and strain energy conversion during unloading were significantly influenced by these two factors. DING et al [19] studied the damage evolution in rock after high-temperature treatment in unloading condition, showing that the temperature effect and confining pressure had a significant influence on the mechanical properties of sandstone. In addition, some other scholars attempted to understand unloading rock mechanics with true-triaxial testing system, by which any one or two of the three principle stresses can be unloaded independently. HE et al [20] and MIAO et al [21] explored the acoustic emission and failure characteristics by carrying out true-triaxial unloading experiments on limestone and granite, providing a helpful method to gain an insight into the characteristics of rock bursts.

Although the study on seepage properties of rock under unloading conditions was relatively rarer than under triaxial loading conditions [22–24], it becomes a start in recent years. FERFERA et al [25] conducted experiments on sandstone under various stress paths and simultaneously measured strain and monophasic permeability changes. It shows that a criterion can be defined in the effective mean stress versus deviatoric stress for the permeability evolution. HU et al [26] measured permeability variation during the triaxial unloading–reloading cyclic tests. They concluded that the intrinsic permeability grew slightly during the unloading phase and the declined more significantly at the reloading phase. YU et al [27] investigated the permeability evolution of sandstone samples under three different stress paths, i.e. conventional triaxial compression, unloading confining pressure at the pre-peak and post-peak strength (with the differential stress remaining at around 80% of the triaxial compressive strength). It is found that the permeability–axial strain increased more rapidly after unloading under confining unloading conditions than under conventional triaxial compression process. In a word, the previous researches deepen the understanding of the mechanical properties and permeability characteristics of rock under various stress paths. However, deformation and permeability change under confining pressure unloading conditions have not been fully discovered, and the essential mechanism requires additional investigation.

This work aims at further exploring the deformation characteristics and permeability properties and providing some parameters to character the rock under unloading conditions. A series of stress–strain curves and permeability changes under confining pressure unloading conditions were obtained during triaxial experiments conducted on sandstone samples, and meanwhile acoustic emission signals in this loading path were real-time monitored. The results were analyzed in detail in order to clarify the intrinsic relationship among variations of the stress–strain

curves, acoustic emission, and permeability evolution.

2 Experimental materials and methods

2.1 Sample preparation

Sandstone was used as experimental material throughout this study, which was collected from Zigong city, Sichuan province, China. The rock cores were prepared in a cylindrical shape with a diameter of 25 mm and a height of 50 mm according to ISRM suggested method [28]. In order to enhance the uniformity of all these samples, they were drilled from adjacent part of a large block without any macroscopic cracks. Both end-faces of these rock samples were carefully polished to ensure the error of unevenness less than 0.05 mm. It was also essential that the end-faces were parallel within a small tolerance, 0.1 mm or less. The sandstone samples achieved in laboratory and a typical SEM photomicrograph of this rock are shown in Figure 1.

Table 1 gives some characteristics of the sandstone samples, including the bulk density, porosity and P-wave velocity. An average bulk density of 2.265 g/cm^3 was determined after drying at 110 °C for 6 h. The porosity values of samples (average value: 8.784%) were measured using the QKY-ZN core porometer (Figure 2(a)) manufactured by China University of Petroleum Instrument Co., Ltd. An assembled testing system (Figure 2(b)), which was composed of a Tektronix 3012 digital phosphor oscilloscope, an Olympus 5077PR pulser receiver, a pair of P-wave transducers and a pair of S-wave transducers with frequency of 500 kHz, was used to measure the P- and S-wave velocities of the samples. The mean values of P- and S-wave velocity were 2796.641 m/s and 1469.934 m/s, respectively. All these characteristics of each sample were within ±5% of their mean value, which ensured the uniformity for subsequent triaxial experiments.

2.2 Testing equipment

Triaxial compression tests were carried out using a home-designed TAW-1000 electro-hydraulic servo controlled testing system. A schematic diagram of the triaxial testing system is shown in Figure 3. This testing system could independently and precisely control the axial load,

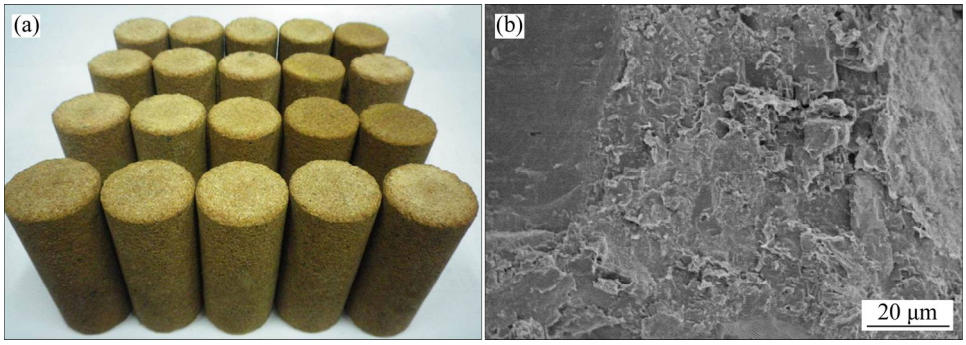

Figure 1 Sandstone samples and a typical SEM picture: (a) Sandstone samples achieved in laboratory; (b) SEM picture

Table 1 Characteristics of sandstone samples

Sample	Diameter/mm	Length/mm	Bulk density/(g·cm^{-3})	Porosity/%	P-wave velocity/(m·s^{-1})	S-wave velocity/(m·s^{-1})
S-10-1	24.96	52.80	2.26	8.63	2796.23	1454.49
S-20-1	24.92	52.78	2.27	9.01	2809.18	1438.05
S-30-1	24.90	52.04	2.23	8.79	2777.92	1504.59
S-10-4	24.82	52.74	2.29	8.50	2838.54	1533.87
S-20-4	25.16	52.10	2.28	8.76	2762.05	1482.52
S-30-4	24.84	52.90	2.27	8.94	2815.62	1427.24
S-10-7	24.92	52.78	2.28	8.85	2792.73	1462.55
S-20-7	24.98	52.18	2.24	8.92	2757.21	1477.83
S-30-7	25.02	52.12	2 29	8.66	2820.29	1448.27
Mean value	—	—	2.265	8.784	2796.641	1469.934

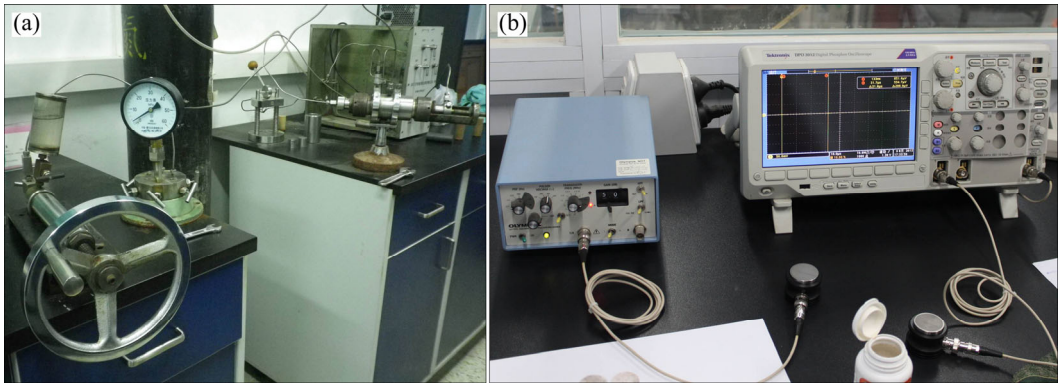

Figure 2 Testing devices of porosity and P- and S-wave velocity: (a) QKY-ZN core porometer for measuring porosity of rock samples; (b) Assembled testing system of acoustic wave velocity

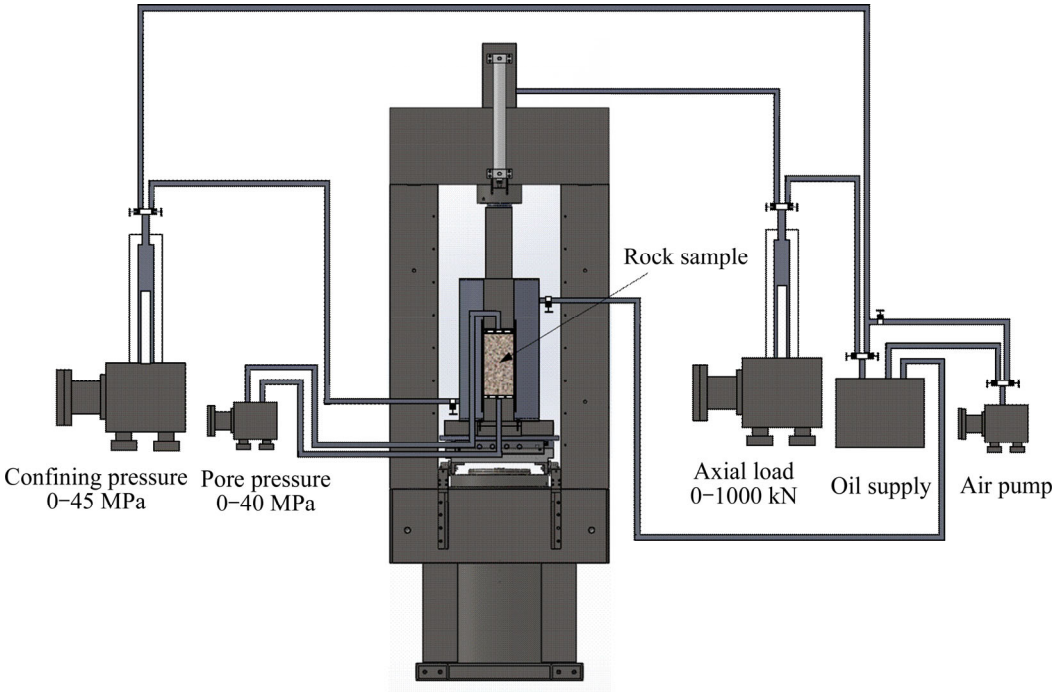

Figure 3 Schematic diagram of triaxial testing system

confining pressure and pore pressure. The maximum axial loading capacity of the system is 1000 kN, and the control accuracy of the axial load is 1 kN. The confining pressure and pore pressure can be respectively increased up to 45 and 40 MPa with a control accuracy of 0.01 MPa. Based on the function of pore pressure control, the system also has the ability to measure permeability evolution of rock sample in the progressive process of triaxial compression. During the experimentation, the axial and radial deformations were measured using two resistor strain type displacement transducers with a measuring accuracy of ±0.001 mm. In addition, the acoustic emission signal was real-time monitored by employing a DISP acoustic emission signal collection system produced by Physical Acoustic Corporation.

2.3 Experimental methods

In this study, a series of confining pressure unloading experiments were performed with the following steps: First, the confining pressure was imposed on the sandstone samples with the hydrostatic pressure (σ_1=σ_3) increasing to the designated value (10, 20 or 30 MPa). Then, the differential stress was incrementally increased at an axial displacement control rate of 0.04 mm/min up to a desired level prior to the peak stress, which was about 80% of the triaxial compressive strength determined from previous conventional triaxial experiments under the same conditions. Finally, the differential stress was maintained constant. At the

same time, the confining pressure was gradually unloaded at a rate of 0.05 MPa/min until the samples failed.

To measure the permeability, a steady water pressure difference between both end-faces of the rock sample, which could drive the water from one end-face to the other, was formed by applying a 1, 4 or 7 MPa water pressure on the top end-face of the sample and linking the bottom end-face to the air. The hydro-mechanical coupling effect would emanate from the combined action of the water pressure inside the rock sample and the axial and radial loads. Eight to ten permeability points were determined to reflect the permeability evolution in the whole loading process. During the measurement, Darcy's law was assumed to be valid, which is described by [9, 29, 30]

$$k = \frac{Q\mu L}{\Delta pA} \tag{1}$$

where k (m^2) is the permeability of the samples; μ is the dynamic viscosity coefficient of water and equals 1.005×10^{-6} kPa·s at room temperature of 20 °C; Q ($m^3\cdot s^{-1}$) is the flow rate through the samples per unit time; L (m) and A (m^2) denote the height and cross-section of the sample, respectively; Δp stands for the pressure difference between the two end-faces of the sample.

During the whole loading process, the acoustic emission signal was real-time monitored with an acoustic emission sensor, of which the threshold was set at 45 dB.

3 Experimental results

3.1 Relationship among stress–strain, acoustic emission and permeability

Figure 4 represents the differential stress–axial strain curves, permeability–axial strain curves and the real-time monitoring results of the acoustic emission energy signal of sandstone samples, which are in the loading path of confining pressure unloading prior to the peak stress and under the respective coupling conditions of confining pressures of 10, 20 and 30 MPa and pore pressures of 1, 4 and 7 MPa. It can be observed from Figure 4 that, under the coupling conditions of different unloading initial confining pressures and pore pressures, the permeability evolution pattern and the characteristic variation of the acoustic emission energy exhibits an identical tendency, and there is a good corresponding relationship between the stress–axial strain curve, permeability–axial strain curve and acoustic emission activity pattern. Several stages can be divided to elaborate these tendencies:

1) In the initial compaction stage, the primary micropores and microcracks in the sandstone samples close gradually. In the course of closure, partial coarse surfaces interlock with each other, producing a small amount of acoustic emission signals with lower energy. At this stage, the permeability continuously decreases with the increasing of axial strain.

2) At the early stage of elastic deformation, the acoustic emission signal is still relatively quiet with little change in the initial compaction stage. This is because the stress at that moment is not large enough to produce new cracks in the rock. The acoustic emission activities are caused by the dislocation between the surfaces of partially closed cracks and slips between the rock grains. At this moment, the sandstone skeleton particles are further squeezed. The flow channels, such as intergranular micropores and microcracks, are further compressed, and apertures of microcracks decrease. The seepage of water inside the rock sample is more difficult, resulting in a continuous decrease in permeability until its bottom value with the increasing of the axial strain.

3) During the middle and late period of the elastic deformation stage, under the coupling effect of pore pressure and confining pressure, the microcracks inside the sandstone sample begin to grow and produce new microcracks. Meanwhile, the acoustic emission activities become more active and the acoustic emission energy continuously increased. At this stage, the permeability starts to go up from its bottom value.

4) After gradually unloading the confining pressure, new microcracks continue to grow and propagate steadily. At this moment, the acoustic emission activities are quite active, and the permeability continues to increase.

5) During the middle and late period of horizontal development of the differential stress–strain curve, the rock sample dilatates, the internal microcracks grow, penetrate and connect, and the acoustic emission activities are highly dense and exhibit an obvious burst signal. The relative

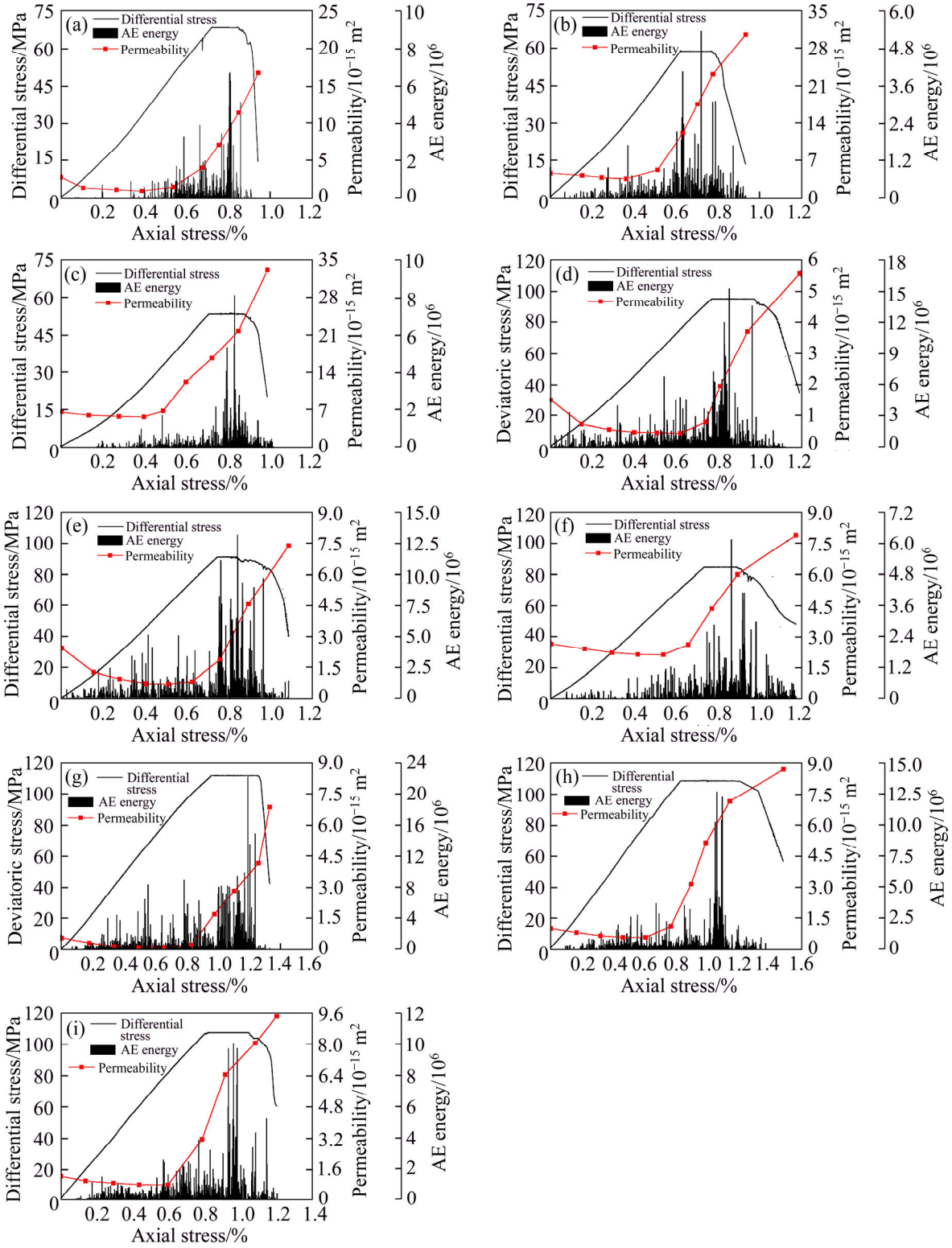

Figure 4 Evolution of differential stress, permeability and acoustic emission energy with axial strain under different pore pressure differences coupling with different confining pressures unloading conditions: (a) Confining pressure of 10 MPa, pore pressure difference of 1 MPa; (b) Confining pressure of 10 MPa, pore pressure difference of 4 MPa; (c) Confining pressure of 10 MPa, pore pressure difference of 7 MPa; (d) Confining pressure of 20 MPa, pore pressure difference of 1 MPa; (e) Confining pressure of 20 MPa, pore pressure difference of 4 MPa; (f) Confining pressure of 20 MPa, pore pressure difference of 7 MPa; (g) Confining pressure of 30 MPa, pore pressure difference of 1 MPa; (h) Confining pressure of 30 MPa, pore pressure difference of 4 MPa; (i) Confining pressure of 30 MPa, pore pressure difference of 7 MPa

magnitude of the burst signal energy is approximately one order of magnitude higher than that of the other deformation stages. At this stage, the permeability dramatically increases, and its magnitude also increases by almost one order of magnitude compared to the minimum permeability measured at the elastic deformation stage.

6) The horizontal development differential stress–strain curve continues for some time, then drops suddenly. During this stage of stress dropping, the acoustic emission energy signal rapidly tends to be quiet. Since the duration of this stage is quite short, only one or two points of permeability can be tested. From the tested results, the permeability at this stage still significantly increases. This is because under the combined application of axial stress, pore pressure and continuously unloaded confining pressure, the microcracks continuously grow, increase and finally form a connected macrocrack, which serves as a main flow channel. The aperture of the macrocrack continues to increase, resulting in the continuously rapid increasing of the permeability [25].

The production of the acoustic emission energy signals is the result of the coupling effect of axial stress, radial stress and pore water pressure. The variation in external axial and radial stress can alter the micropores, microcracks and other internal structures of sandstone, which will produce acoustic emission signals; on the other hand, the pressure difference of water flow inside the sandstone sample acts on the microcrack surfaces, which can lead to the tensile cracks of the microstructures of the sandstone, leading to production of acoustic emission signals. The acoustic emission signal reflected the variation of the internal structure of the rock sample, and the internal structural variation is the fundamental cause that determines the changing pattern of the permeability. From the distribution acoustic emission energy signals in the whole stress–strain process, only part of strain energy stored in the rock sample is released at the first four stages and the burst acoustic emission signals appear at the fifth stage, in which the confining pressure is unloaded to a certain extent. The appearance of burst acoustic emission signals is similar to the sudden release of energy in the actual rock engineering, i.e. rock burst, which is also induced by excavation of surrounding rock with high ground stress in some deep rock engineering. The appearance of burst signals marks severe damage occurring inside the rock sample, heralding that failure is about to occur and the rock sample is about to lose its bearing capacity.

From Figure 4, the changing pattern of the permeability evolution does not change with the variation in confining pressure and pore pressure and exhibited '√'-shaped changes. However, the relative values of permeability in all deformation stages vary. This is reflected by the fact that under the same initial confining pressure, the higher the pore pressure, the higher the permeability at the various deformation stages. In contrast, the lower the pore pressure, the lower the permeability at the various deformation stages. This observation can be explained as follows: the stress intensity factor of the microcracks tips inside the rock decreases due to the pore pressure which also weakens the bonding capacity between particles; in addition, the rock is softened because water dissolves many mineral compositions in the rock. Thus, the microcracks inside the rock propagate significantly so as to improve the permeability of the rock. Under the same pore pressure, the impact of confining pressure on permeability is primarily represented by the observation that a higher confining pressure correlates with a lower permeability; on the contrary, a lower confining pressure correlates with a higher relative permeability. From the concept of effective confining pressure, it can be concluded that the relative values of permeability at various deformation stages of the rock sample are negatively correlated with effective confining pressure. This is because a higher effective confining pressure compresses the micropores and microcracks inside the rock samples and limits the opening of the microcracks. Thus, the flow channels decrease and inhibit the seepage.

In addition, Table 2 provides the experimental conditions and the first values on permeability evolution curves. It can be seen from Table 2 that the first point on the permeability evolution curve changes with the confining pressure and pore pressure difference under the coupling conditions. For the same confining pressure, the first values on permeability evolution curves gradually increase with the increase in pore pressure, but the increasing amplitude is relatively small. When the pore pressure remains the same and the confining

Table 2 Experimental conditions and first values on permeability evolution curves

Sample	Confining pressure before unloading/MPa	Pore pressure difference/MPa	Mean pore pressure along height direction/MPa	Effective confining pressure/MPa	The first value on permeability evolution curve/10^{-15} m^2
S-10-1	10	1.0	0.5	9.5	2.836
S-20-1	20	1.0	0.5	19.5	1.489
S-30-1	30	1.0	0.5	29.5	0.562
S-10-4	10	4.0	2.0	8.0	4.506
S-20-4	20	4.0	2.0	18.0	2.402
S-30-4	30	4.0	2.0	28.0	1.005
S-10-7	10	7.0	3.5	6.5	6.421
S-20-7	20	7.0	3.5	16.5	2.647
S-30-7	30	7.0	3.5	26.5	1.163

pressure increases, the first values on permeability evolution curves gradually decrease with large decreasing amplitude. This observation indicates that the first values on permeability evolution curves are highly affected by the confining pressure but little affected by the pore pressure. In employing Darcy's law, it is assumed that there is a linear pressure gradient across the rock sample [31]. With reference to the principle of effective stress [32], the effective confining pressure can be calculated, which is also listed in Table 2. Thus, it can be concluded that the first value on permeability evolution curve gradually decreased with the increase in effective confining pressure.

3.2 Deformation characteristics

Figure 5 illustrates the stress–axial strain, stress–radial strain and stress–volumetric strain curves under confining pressure unloading conditions. It can be seen from this figure that, after the confining pressure is unloaded, the radial strain grows much faster than the axial strain qualitatively, which induces the volumetric strain also growing rapidly. To further quantitatively analyze the deformation characteristics of sandstone samples under confining pressure unloading conditions, a variable presented as strain–confining pressure compliance, which was first proposed by QIU et al [33], is introduced. The strain–confining pressure compliance $\Delta\dot{\varepsilon}_i$ is defined as the ratio of strain increment to confining pressure reduction between the start point of confining pressure unloading and the point of stress dropping, which can be written as

$$\Delta\dot{\varepsilon}_i = \frac{\Delta\varepsilon_i}{\Delta\sigma_3} \tag{2}$$

where $\Delta\dot{\varepsilon}_i$ (i=1, 3, or v) are axial, radial or volumetric strain–confining pressure compliance; $\Delta\varepsilon_i$ (i=1, 3, or v) are axial, radial or volumetric strain increment, respectively; $\Delta\sigma_3$ is the confining pressure reduction. The strain–confining pressure compliance is the physical quantities reflecting the influential effect of confining pressure variation on deformation in the process of confining pressure unloading. The larger the value of the strain–confining pressure compliance is, the more sensitively the deformation changes with the confining pressure variation. Table 3 gives the values of axial, radial, and volumetric strain-confining pressure compliance for the rock samples in this study. From this table, it can be seen that the value of radial strain–confining pressure compliance is greater than the value of axial strain–confining pressure compliance for each rock sample, and the value of volumetric strain-confining pressure compliance is the largest among these three groups of data. Thus, the radial deformation is much more sensitive to confining pressure reduction than the axial deformation, and it quantitatively reveals that the rapid dilatancy of the rock sample after confining pressure unloading is mainly induced by significant increase in radial deformation.

Figure 6 shows the history curve between the radial strain (the direction of positive strain is used to point outwards herein) and its corresponding confining pressure measured during the entire course of unloading confining pressure path for rock samples under various pore pressure differences set in the experiments. It is thus observed that the radial strain gradually increases with the decrease in confining pressure. During the

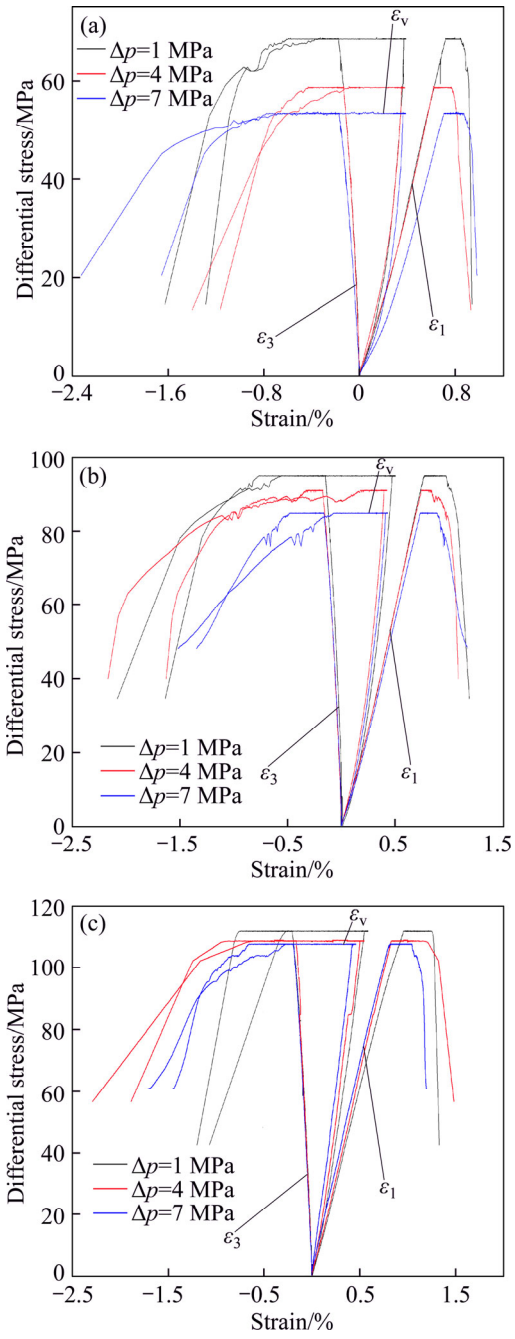

Figure 5 Stress–strain curves for sandstone under confining pressure unloading conditions: (a) Confining pressure of 10 MPa; (b) Confining pressure of 20 MPa; (c) Confining pressure of 30 MPa

early stage of confining pressure unloading, the radial strain increases slightly and in an approximately linear relationship. However, with a further decrease in the confining pressure, the radial strain rapidly increases, and the radial strain develops into a non-linear relationship with the confining pressure. At this moment, rock samples exhibit a non-recoverable plastic deformation. The microcracks in the rock samples form, grow and connect gradually and finally result in failure. In addition, it also can be seen from Figure 6 that, at the same confining pressure before unloading, with an increase in pore pressure difference, the curve gradually moves up, indicating a larger final value of confining pressure corresponding to the failure.

Table 3 Axial, radial and volumetric strain–confining pressure compliance for samples

Sample	Compliance		
	Axial strain–confining pressure	Radial strain–confining pressure	Volumetric strain–confining pressure
S-10-1	2.90×10^{-4}	1.24×10^{-3}	2.19×10^{-3}
S-20-1	2.28×10^{-4}	5.37×10^{-4}	8.45×10^{-4}
S-30-1	1.88×10^{-4}	7.74×10^{-4}	1.36×10^{-3}
S-10-4	1.52×10^{-4}	5.18×10^{-4}	8.85×10^{-4}
S-20-4	1.93×10^{-4}	7.92×10^{-4}	1.39×10^{-3}
S-30-4	6.81×10^{-4}	1.52×10^{-3}	2.37×10^{-3}
S-10-7	1.62×10^{-4}	3.52×10^{-4}	5.43×10^{-4}
S-20-7	2.75×10^{-4}	6.50×10^{-4}	1.03×10^{-3}
S-30-7	3.46×10^{-4}	9.70×10^{-4}	1.59×10^{-3}
Mean value	2.794×10^{-4}	8.170×10^{-4}	1.356×10^{-3}

Regardless of the magnitude of difference in the confining pressure and pore pressure, these nine groups of rock samples primarily failed by shearing failure, and a single macro shear failure surface formed. A typical macro failure mode for a sandstone sample under the loading path of unloading confining pressure prior to the peak stress in this experiment is shown in Figure 7. These two photos illustrate that the failure mode under confining pressure unloading condition belongs to brittle failure, and the macro fracture appearance under the confining pressure unloading conditions exhibits irregular forms, and the cuts are not flat or even. The differential stress is constant, but the decrease in confining pressure alters the stress state. The radial strain of the rock sample dramatically increases and continues to dilatate and finally results in the brittle shear failure of the rock samples.

3.3 Deformation parameter analysis

Generally speaking, the deformation parameters of rock, such as elasticity modulus, deformation modulus, and Poisson ratio, are obtained from uniaxial compressive test. For triaxial compression in the loading path of

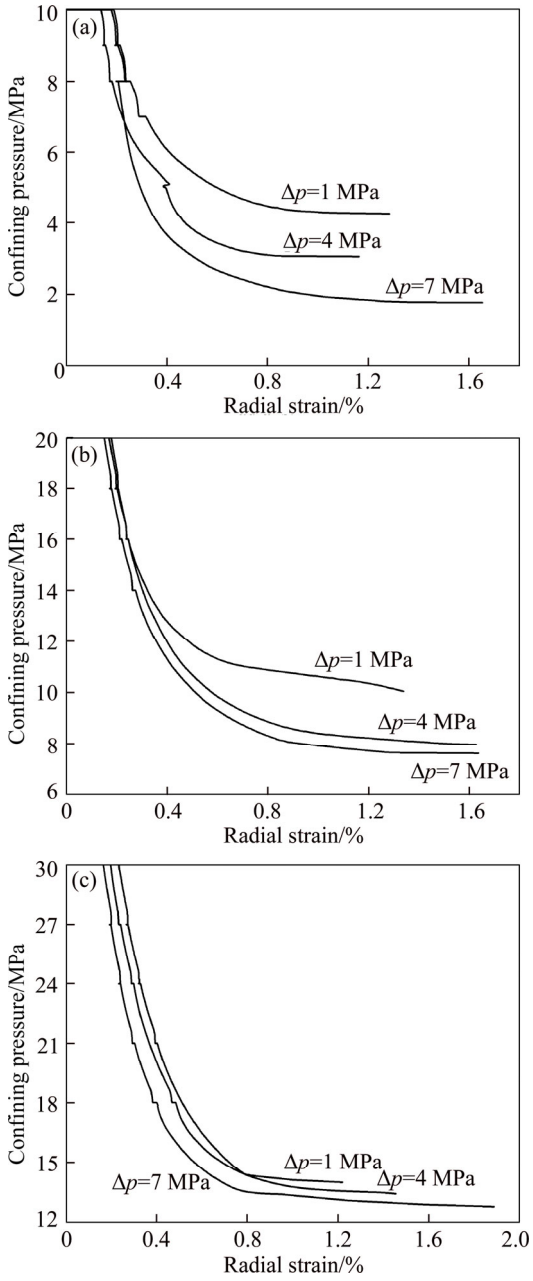

Figure 6 Variation in confining pressure with radial strain under confining pressure unloading conditions: (a) Initial confining pressure of 10 MPa; (b) Initial confining pressure of 20 MPa; (c) Initial confining pressure of 30 MPa

Figure 7 Typical pictures of failure pattern under confining pressure unloading condition

confining pressure unloading, the deformation modulus E and Poisson ratio μ can be calculated by the following formulas:

$$E=\frac{\sigma_1-2\mu\sigma_3}{\varepsilon_1} \tag{3}$$

$$\mu=\frac{B\sigma_1-\sigma_3}{\sigma_3(2B-1)-\sigma_1} \tag{4}$$

$$B=\frac{\varepsilon_3}{\varepsilon_1} \tag{5}$$

where σ_1, σ_3 are axial stress and confining pressure in the confining pressure unloading process, respectively; ε_1, ε_3 are axial and radial strain, respectively.

Figure 8 shows the relationship between confining pressure and deformation modulus under confining pressure unloading conditions. From Figure 8, it can be seen that the deformation modulus decreases with the unloaded confining pressure. Based on damage mechanics [34, 35], the damage variable D is evaluated as:

$$D=1-\frac{E}{E_0} \tag{6}$$

where E and E_0 are elastic modulus of undamaged material and damage elasticity modulus, respectively. To describe the degradation process of confining pressure unloading, the equation is extended as

$$D=1-\frac{E_{\mathrm{u}}}{E_{\mathrm{s}}} \tag{7}$$

where E_{u} represents the deformation modulus of the rock sample during confining pressure unloading process, and E_{s} is the deformation modulus at start point of confining pressure unloading. Thus, with the decrease in deformation modulus during the confining pressure unloading process, the damage variable D gradually increases, indicating that confining pressure unloading is a process of damage accumulation and strength degradation.

The degree of difficulty associated with the unloading confining failure for sandstone differed with respect to various confining pressures and pore pressure differences coupling conditions. For this reason, a reduction rate of confining pressure β is defined to reflect the degree of difficulty of rock sample failure. Here the β is written as

$$\beta=\frac{\sigma_0-\sigma_3'}{\sigma_0} \tag{8}$$

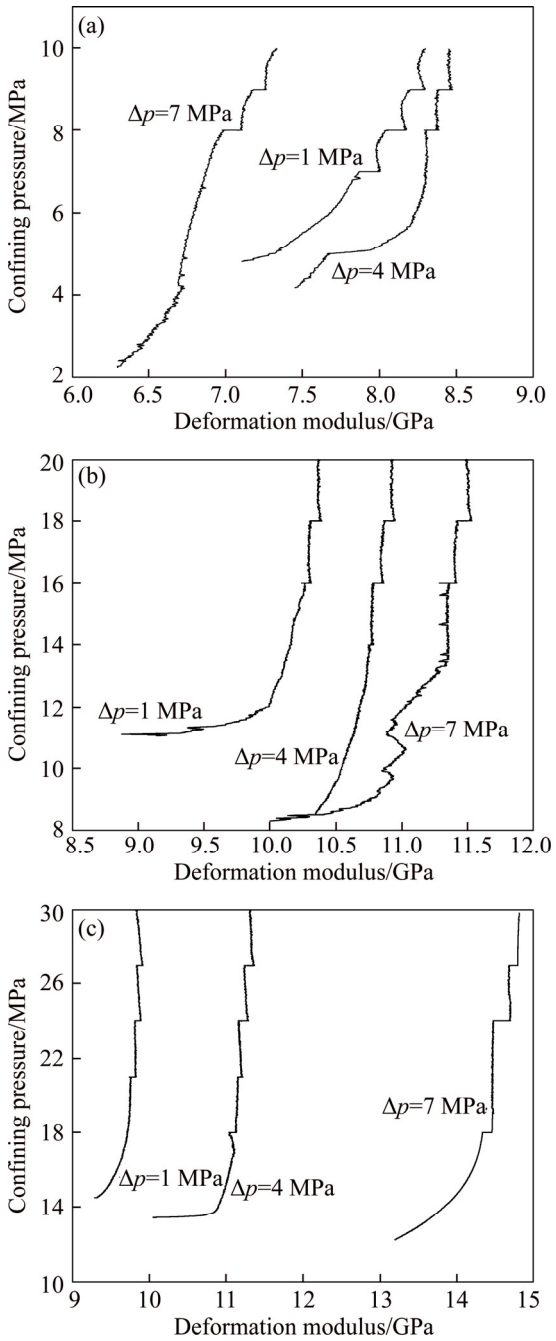

Figure 8 Relationship between confining pressure and deformation modulus under confining pressure unloading conditions: (a) Initial confining pressure of 10 MPa; (b) Initial confining pressure of 20 MPa; (c) Initial confining pressure of 30 MPa

where σ_0 is confining pressure before unloading; σ_3' is the final value of confining pressure corresponding to the failure.

Table 4 gives the characteristic values of the unloading confining pressure failure. It is observed from Table 4 that when the confining pressure is unloaded to 22.5%–48.3% of the initial confining pressure, the rock sample fails suddenly. In addition, in combination with the relationship between the reduction rate of confining pressure β and the pore pressure difference presented in Figure 9, it is visually observed that for the same confining pressure, the smaller the pore pressure is, the larger the confining pressure corresponding to failure is, the smaller the β value is, the lower the degree of confining pressure unloading is, and the easier the rock sample fails; however, from the view of the same pore pressure, the β value does not show an obvious change with the change in confining pressure.

Table 4 Characteristic values of unloading confining pressure failure

Sample	Confining pressure before unloading, σ_0/MPa	Final value of confining pressure corresponding to failure, σ'_3/MPa	(σ'_3/σ_0)/%	Reduction rate of confining pressure, β/%
S-10-1	10	4.81	48.1	51.9
S-20-1	20	8.54	42.7	57.3
S-30-1	30	14.49	48.3	51.7
S-10-4	10	4.18	41.8	58.2
S-20-4	20	8.30	41.5	58.5
S-30-4	30	13.4	44.7	55.3
S-10-7	10	2.25	22.5	77.5
S-20-7	20	8.22	41.1	58.9
S-30-7	30	12.22	40.8	59.2

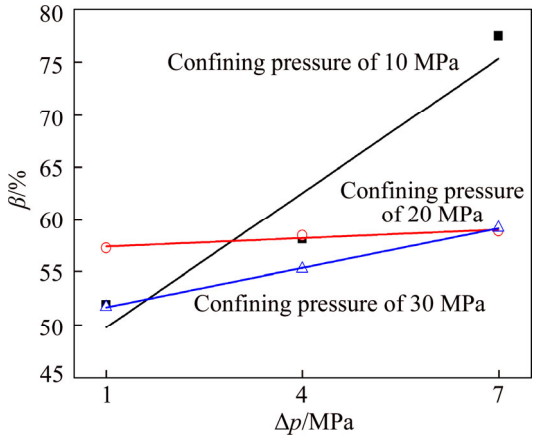

Figure 9 Relationship between reduction rate of confining pressure β and pore pressure difference

3.4 Relationship between permeability and volumetric strain

Figure 10 shows the relationship between the permeability and volumetric strain under the coupling conditions of unloading confining pressures and pore pressure differences. The

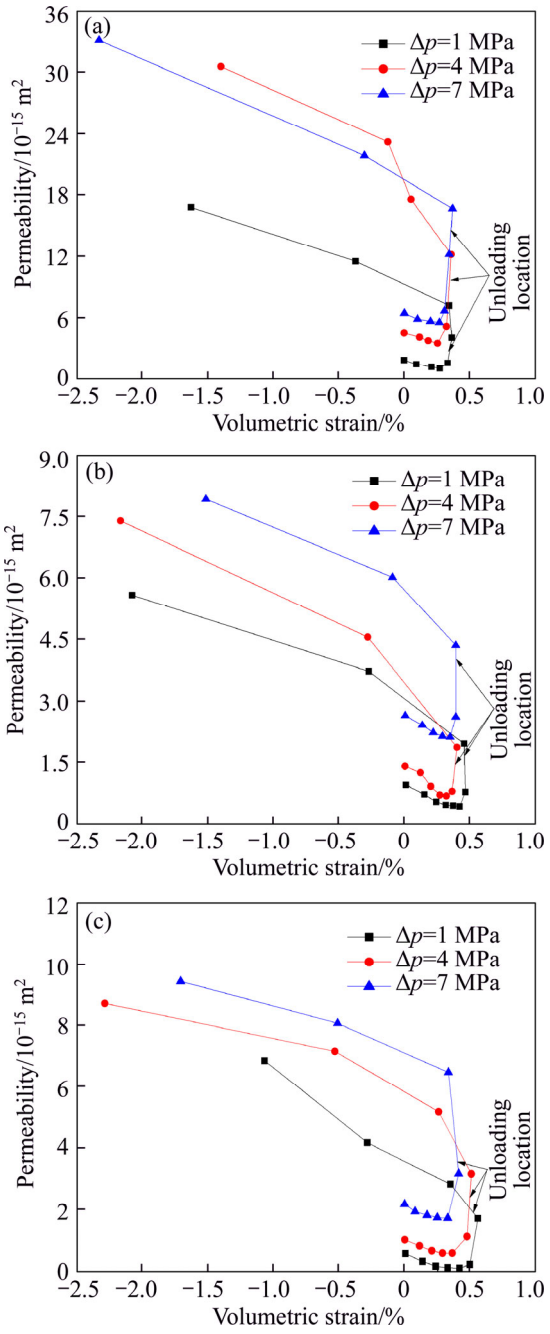

Figure 10 Relationship between permeability and volumetric strain under confining pressure unloading conditions: (a) Initial confining pressure of 10 MPa; (b) Initial confining pressure of 20 MPa; (c) Initial confining pressure of 30 MPa

unloading location set in this experiment was correlated to about 80% of the triaxial compression strength and was close to the critical location where the rock sample was going to change from linear deformation to non-linear deformation. As shown by the arrow in Figure 10, the unloading location is approximately at the limited state of contraction, namely, where the volumetric strain reaches the maximum positive value. The volumetric compression of the rock sample is quite slow (the variation of the volumetric strain of the unit axial strain is relatively small) before the confining pressure is unloaded. The volumetric strain gradually changes from positive to negative after the confining pressure is unloaded, namely, the rock samples change from the volumetric compression state into the volumetric expansion state and exhibit a rapid rate (the variation in the volumetric strain of the unit axial strain is relatively large).

From the entire loading and unloading process, there is a certain positive correlation between the permeability and volumetric strain. Before confining pressure unloading, under the coupling applications of axial stress, confining pressure and pore pressure, the volume of the rock sample is compressed, and the permeability decreases slightly; after the confining pressure unloading, the volume of the rock sample is dilatated significantly, and the permeability increased dramatically. This is because the permeability is closely related to the variation in the internal structure of the rock. When the rock is compressed, its internal micropores and microcracks providing the seepage channel are contracted, and the seepage channel shrinks, leading to difficulty of water passing through the rock sample in unit time under constant coupling condition of confining pressure and pore pressure. In contrast, after the confining pressure is unloaded, the radial strain dramatically increases, which consequently results in a dramatic increase in volumetric strain. At this moment, the microcracks and micropores continue to newly initiate, grow, propagate, connect, and benefit for the seepage of fluid in the rock samples. Meanwhile, compared to the former context, the intense stage of acoustic emission activity occurs after volumetric dilatation. This means that the intensive energy released from the rock sample is the result of internal microcracks growth, penetration and convergence.

Observations of the limit location of volumetric compression and the location of the minimum permeability show that they do not completely correspond to each other. The minimum point of the permeability lags the limit point of volumetric compression. WU et al [36] reported that the initiation of microfractures for hardy sandstone was about 64.5% of the peak stress. This means that before loading to 64.5% of the peak

stress, the microfractures initiate and grow slowly; after reaching this threshold value, the microfractures initiate and grow rapidly. In Figure 10, the minimum value of the permeability occurs before the onset of dilatancy of the sample. From the view of microfractures initiation, it is found that the minimum value of the permeability occurs close to the threshold value of microfractures initiation. After reaching the threshold value, a large number of rapidly initiating and growing microfractures create new seepage channels, which provide more abundant seepage paths for fluid in the rock samples and result in the improvement of the permeability of the rock sample. Comparing the initial permeability measured at the zero point of volumetric strain at the early stage of compression and at the dilatancy stage, it is found that although the rock is compressed and then expanded to zero volumetric strain, the permeability is much larger than the initial permeability measured at the early stage of compression. This is because the cumulative damage inside the rock, which is induced by microfractures initiation and growth under the application of the external load, resulted in porosity, distribution and a number of cracks different from those at the initial state of the rock sample.

4 Conclusions

For the Sichuan sandstone rock samples, this research utilized the rock mechanics electro-hydraulic servo controlled testing system to carry out confining pressure unloading experiments with the initial confining pressures of 10, 20 and 30 MPa, and pore pressure differences of 1, 4 and 7 MPa. The following conclusions are summarized.

1) In the initial compaction stage and the early stage of elastic deformation, a small number of acoustic emission signals with lower energy were produced with the increasing of axial strain. Then, they became more active with increasing energy. When confining pressure was unloaded, the acoustic emission activities became quite active, and tended to be quiet again at the stage of stress dropping.

2) The changing pattern of the permeability evolution did not change with the variation in initial confining pressure and pore pressure and exhibited '√'-shaped changes, but the relative values of permeability in all deformation stages varied. With the increase in effective confining pressure, the initial permeability of the rock sample gradually decreased, and the permeability at various deformation stages was smaller.

3) After the confining pressure was unloading, the radial strain grew much faster than axial strain, which induced the volumetric strain growing rapidly. This phenomenon could be quantitatively evaluated by the concept of the strain–confining pressure compliance.

4) All failures under confining pressure unloading conditions featured brittle failure, and the failure mode was shear failure with a single macro shear rupture surface.

5) With the decrease in deformation modulus during the confining pressure unloading process, the damage variable D gradually increased, indicating that confining pressure unloading was a process of damage accumulation and strength degradation. A reduction rate of confining pressure β could be defined to reflect the degree of difficulty of rock sample failure.

6) From the entire loading and unloading process, there is a certain positive correlation between the permeability and volumetric strain.

References

[1] COOK P. In situ pneumatic testing at yucca mountain [J]. International Journal of Rock Mechanics and Mining Sciences, 2000, 37(1): 357–367. DOI: 10.1016/S1365-1609(99)00111-2.

[2] WANG J. High-level radioactive waste disposal in China: update 2010 [J]. Journal of Rock Mechanics and Geotechnical Engineering, 2010, 2(1): 1–11. DOI: 10.3724/SP.J.1235.2010.00001.

[3] WANG J. On area-specific underground research laboratory for geological disposal of high-level radioactive waste in China [J]. Journal of Rock Mechanics and Geotechnical Engineering, 2014, 6(2): 99–104. DOI: 10.1016/j.jrmge.2014.01.002.

[4] JOW H. Current status of the United States spent nuclear fuel disposition research and development [J]. World Nuclear Geoscience, 2014, 31(S1): 497–498. http://kns.cnki.net/KCMS/detail/detail.aspx?dbcode=CPFD&dbname=CPFD0914&filename=ZGYJ201408001062&v=MjU2NzBHNEg5WE1wNDlGWmVzSkRoTkt1aGRobmo5OFRuanFxeGRFZU1PVUtyaWZadTV2RXl2a1VML0lLVjhSUHlyU1pM.

[5] TANG Y, YANG R, BIAN X. A review of CO_2 sequestration projects and application in China [J]. The Scientific World Journal, 2014, 2014(6): ID 381854. DOI: 10.1155/2014/381854.

[6] FANG Y, WANG C, ELSWORTH D, ISHIBASHI T. Seismicity-permeability coupling in the behavior of gas shales, CO_2, storage and deep geothermal energy [J]. Geomechanics and Geophysics for Geo-Energy and Geo-Resources, 2017, 3(2):1–10. DOI: 10.1007/s40948-017-0051-9.

[7] ZHANG Y, LU W, CHEN M, YAN P, HU P. Dam foundation excavation techniques in China: A review [J]. Journal of Rock Mechanics and Geotechnical Engineering, 2013, 5(6):460–467. DOI: 10.1016/j.jrmge.2013.08.002.

[8] LI S, FENG X T, LI Z, CHEN B, ZHANG C, ZHOU H. In situ, monitoring of rockburst nucleation and evolution in the deeply buried tunnels of Jinping II hydropower station [J]. Engineering Geology, 2012, 137–138(7): 85–96. DOI: 10.1016/j.enggeo. 2012.03.010.

[9] BRACE W F, WALSH J B, FRANGOS W T. Permeability of granite under high pressure [J]. Journal of Geophysical Research, 1968, 73(6): 2225–2236. DOI: 10.1029/ JB073i006p02225.

[10] WALSH J B. Effect of pore pressure and confining pressure on fracture permeability [J]. International Journal of Rock Mechanics and Mining Sciences & Geomechanics Abstracts, 1981, 18(5): 429–435. DOI: 10.1016/0148-9062(81)90006-1.

[11] ODA M, TAKEMURA T, AOKI T. Damage growth and permeability change in triaxial compression tests of Inada granite [J]. Mechanics of Materials, 2002, 34(6): 313–331. DOI: 10.1016/S0167-6636(02)00115-1.

[12] PATERSON M S, WONG T F. Experimental rock deformation–the brittle field [M]. Germany: Springer, 2005.

[13] HOKKA M, BLACK J, TKALICH D, FOURMEAU M, KANE A, AOANG N H, LI C C, CHEN W W, KUOKKALA V T. Effects of strain rate and confining pressure on the compressive behavior of Kuru granite [J]. International Journal of Impact Engineering, 2016, 91: 183–193. DOI: 10.1016/j.ijimpeng.2016.01.010.

[14] HUANG R Q, WANG X N, CHAN L S. Triaxial unloading test of rocks and its implication for rock burst [J]. Bulletin of Engineering Geology and the Environment, 2001, 60(1): 37–41. DOI: 10.1007/s100640000082.

[15] HUA A Z, YOU M Q. Rock failure due to energy release during unloading and application to underground rock burst control [J]. Tunnelling and Underground Space Technology, 2001, 16(3): 241–246. DOI: 10.1016/S0886-7798(01)00046-3.

[16] LIU Q, CHENG Y, JIN K, TU Q, ZHAO W, ZHANG R. Effect of confining pressure unloading on strength reduction of soft coal in borehole stability analysis [J]. Environmental Earth Sciences, 2017, 76(4): 173. DOI: 10.1007/s12665-017-6509-9.

[17] LIANG Y, LI Q, GU Y, ZOU Q. Mechanical and acoustic emission characteristics of rock: Effect of loading and unloading confining pressure at the postpeak stage [J]. Journal of Natural Gas Science & Engineering, 2017, 44: 54–64. DOI: 10.1016/j.jngse.2017.04.012.

[18] HUANG D, LI Y. Conversion of strain energy in triaxial unloading tests on marble [J]. International Journal of Rock Mechanics & Mining Sciences, 2014, 66(1): 160–168. DOI: 10.1016/j.ijrmms.2013.12.001.

[19] DING Q L, JU F, MAO X B, MA D, YU B Y, SONG S B. Experimental investigation of the mechanical behavior in unloading conditions of sandstone after high-temperature treatment [J]. Rock Mechanics and Rock Engineering, 2016, 49(7): 2641–2653. DOI: 10.1007/s00603-016-0944-x.

[20] HE M C, MIAO J L, FENG J L. Rock burst process of limestone and its acoustic emission characteristics under true-triaxial unloading conditions [J]. International Journal of Rock Mechanics and Mining Sciences, 2010, 47(47): 286–298. DOI: 10.1016/j.ijrmms.2009.09.003.

[21] MIAO J L, JIA X N, CHENG C. The failure characteristics of granite under true triaxial unloading condition [J]. Procedia Engineering, 2011, 26(Complete): 1620–1625. DOI: 10.1016/j.proeng.2011.11.2346.

[22] RICE T L, NICHOLS R W, OLSEN H W. Low gradient permeability measurements in a triaxial system [J]. Géotechnique, 1985, 35(3): 459. DOI: 10.1680/geot. 1985.35.2.145.

[23] HEILAND J. Permeability of triaxially compressed sandstone: influence of deformation and strain-rate on permeability [J]. Pure and Applied Geophysics, 2003, 160(5): 889–908. DOI: 10.1007/PL00012571.

[24] DAVY C A, SKOCZYLAS F, BARNICHON J D, LEBOW P. Permeability of macro-cracked argillite under confinement: Gas and water testing [J]. Physics & Chemistry of the Earth Parts A/B/C, 2007, 32(8–14): 667–680. DOI: 10.1016/ j.pce.2006.02.055.

[25] FERFERA F M R, SARDA J P, BOUTÉCA M, VINCKÉ O. Experimental study of monophasic permeability changes under various stress paths [J]. International Journal of Rock Mechanics and Mining Sciences, 1997, 34(97): 37.e1–37.e12. DOI: 10.1016/S1365-1609(97) 00087-7.

[26] HU D W, ZHOU H, ZHANG F, SHAO J F. Evolution of poroelastic properties and permeability in damaged sandstone [J]. International Journal of Rock Mechanics and Mining Sciences. 2010, 47(6): 962–973. DOI: 10.1016/ j.ijrmms.2010.06.007.

[27] YU J, LI H, CHEN X, CAI Y Y, MU K, ZHANG Y Z, WU N. Experimental study of permeability and acoustic emission characteristics of sandstone during processes of unloading confining pressure and deformation [J]. Chinese Journal of Rock Mechanics and Engineering, 2014, 33(1): 69–79. http://www. rockmech.org/ EN/Y2014/V33/I1/69. (in Chinese)

[28] FAIRHURST C E, HUDSON J A. Draft ISRM suggested method for the complete stress–strain curve for the intact rock in uniaxial compression [J]. International Journal of Rock Mechanics and Mining Sciences, 1999 36(3): 279–289. DOI: 10.1016/0148-9062(87)91231-9.

[29] WYCKOFF R D, BOTSET H G, MUSKAT M, REED D W. The measurement of the permeability of porous media for homogeneous fluids [J]. Review of Scientific Instruments, 1933, 4(7): 394–405. DOI: 10.1063/1.1749155.

[30] JIA C J, XU W Y, WANG H L, WANG R B, YU J, YAN J. Stress dependent permeability and porosity of low-permeability rock [J]. Journal of Central South University, 2017, 24(10): 2396–2405. DOI: 10.1007/s11771-017-3651-1.

[31] ZOBACK M D, BYERLEE J D. The effect of microcrack dilatancy on the permeability of westerly granite [J]. Journal

of Geophysical Research Atmospheres, 1975, 80(5): 752–755. DOI: 10.1029/JB080i005p00752.

[32] BIOT M A. General theory of three-dimensional consolidation [J]. Journal of Applied Physics, 1941, 12: 155–164. http://pdfs.semanticscholar.org/20aa/1691c248a5585a49db224411150af8b7fed1.pdf.

[33] QIU S L, FENG X T, ZHANG C Q, ZHOU H, SUN F. Experimental research on mechanical properties of deep-buried marble under different unloading rates of confining pressures [J]. Chinese Journal of Rock Mechanics and Engineering, 2010, 29(9): 1807–1817. http://www.rockmech.org/ EN/abstract/ abstract20267.shtml. (in Chinese)

[34] LEMAITRE J. A continuous damage mechanics model for ductile fracture [J]. Journal of Engineering Materials and Technology, 1985, 107(1): 83–89. DOI: 10.1115/1.3225775.

[35] LEMAITRE J, DESMORAT R. Engineering damage mechanics: ductile, creep, fatigue and brittle failures [M]. Germany: Springer, 2005.

[36] WU Y Q, CAO G Z. WANG D W. Microfraturing process of rock by real-time observation of X-ray CT [J]. Chinese Journal of Applied Mechanics, 2005, 22(3): 484–490. DOI: 10.3969/j.issn.1000-4939.2005.03.034. (in Chinese)

(Edited by YANG Hua)

中文导读

围压卸载条件下岩石的变形特性及渗透演化的试验研究

摘要：在应力释放条件下岩石的变形行为及水力性质是影响岩石工程开挖及使用安全的两个主要因素，鉴于此，本文以探寻卸荷条件下岩石的变形行为和渗透特性并提供一些表征岩石卸荷性质的参数为研究目标。首先，进行了一组加载路径为应力峰值前卸载围压的三轴试验，在试验中进行渗透率测试及声发射实时信号监测。然后，基于试验结果对整个应力–应变过程中岩石的变形行为及渗透演化情况作了深入分析。结果表明：在围压卸载条件下，岩石的应力–轴向应变曲线、渗透率–轴向应变曲线以及声发射事件分布情况具有很好的对应关系；在围压卸载之后，径向应变发展速率较轴向应变快，从而导致体积应变也迅速增大；所有的卸围压破坏均表现为具有一个宏观破裂面的剪切破坏；随着围压卸载过程中变形模量的不断降低，损伤变量呈不断增加趋势，表明围压卸载过程是一个累积损伤及强度劣化的过程；从整个加载和卸载过程来看，渗透率与体积应变存在一定的正相关关系。

关键词：卸荷岩石力学；渗透演化；三轴试验；声发射；砂岩